ACS Sustainable Chemistry & Engineering

Research Article

pubs.acs.org/journal/ascecg

Relating Electron Donor and Carboxylic Acid Anchoring Substitution Effects in Azo Dyes to Dye-Sensitized Solar Cell Performance

Lei Zhang,[†] Jacqueline M. Cole,*[,†,‡,§] Paul G. Waddell,[†,‡] Kian S. Low,[†] and Xiaogang Liu[†]

[†]Cavendish Laboratory, University of Cambridge, J. J. Thomson Avenue, Cambridge CB3 0HE, United Kingdom

[‡]Department of Chemistry, and [§]Department of Physics, University of New Brunswick, P.O. Box 4400, Fredericton, NB, E3B 5A3 Canada

Supporting Information

ABSTRACT: The relationship between the molecular structures of a series of azo dyes and their operational performance when applied to dye-sensitized solar cells (DSSCs) is probed via experimental and computational analysis. Seven azo dyes, with three different donating groups (dimethylamino, diethylamino, and dipropylamino) and carboxylic acid anchoring positions (*ortho*-, *meta*-, and *para*-substituted phenyl rings) are studied. Single-crystal X-ray diffraction is employed in order to analyze the effects of conformation and quantify the contribution of quinoidal resonance forms to the intramolecular charge transfer (ICT), which controls their intrinsic photovoltaic potential from an electronic standpoint. Harmonic oscillator stabilization energy (HOSE) calculations indicate that the *para*- and *ortho*-azo dyes exhibit potential for DSSC application. However, from a geometrical standpoint, the crystal structure data, proton nuclear magnetic resonance spectroscopy (^{1}H NMR), and density functional theory (DFT) all indicate that intramolecular hydrogen bonds form in *ortho*-dyes within both solid and solution states, impeding their intrinsic ICT-based photovoltaic potential, and offering insights into the photostability of azo dyes and the dye···TiO_2 anchoring mechanism in DSSCs. Donor effects are manifested in the packing mode and molecular planarity revealed by X-ray crystallography and in the UV/vis absorption spectra. DFT and time-dependent density functional theory (TDDFT) were performed to understand the electronic and optical properties of these azo dyes; these calculations compare well with experimental findings. Operational tests of DSSCs, functionalized by these azo dyes, show that the carboxylic acid anchoring position plays a crucial role in DSSC performance, while donating groups offer a much less obvious effect on the overall DSSC device efficiency.

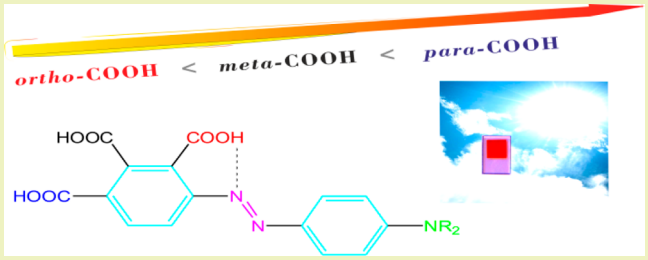

KEYWORDS: *Azo dye, Dye-sensitized solar cell, Intramolecular hydrogen bond, ^{1}H NMR, DFT, TDDFT, HOMO, LUMO, Optoelectronic material*

INTRODUCTION

Dye-sensitized solar cells (DSSCs) have been actively studied since their discovery in the early 1990s.[1] DSSCs mimic natural photosynthesis, using a UV/vis optical absorber, the dye, to absorb light and convert it to electrical power.[2] Historically, ruthenium-based dyes have been employed in the DSSC field.[3−6] However, organic dyes are becoming more and more attractive as alternate light sensitizers because they are much cheaper, more environmental friendly, and have higher molecular-extinction coefficients than their metal−organic counterparts.[7−9] By realizing the molecular structures of these organic dyes and relating them to their UV/vis spectral response and DSSC device operational performance, corresponding structure−property relationships can be developed and rationalized. To this end, UV/vis absorption spectra, HOMO and LUMO energy levels, and intramolecular charge transfer (ICT) pathways in organic dyes can be adjusted systematically by the judicious manipulation of their donor-π-acceptor features.[10−14]

The donor-bridge-acceptor system (D-π-A) in a dye has been identified to be a key molecular dye design criterion for DSSCs,[15] although some modifications such as donor-acceptor-bridge-acceptor (D-A-π-A) exist.[16] ICT from donor to acceptor in a dye is critically important to guarantee proper solar cell functionality.[17,18] Associated HOMO and LUMO charge distributions are ideally localized in donor and acceptor regions respectively in order to strengthen the electron push−pull effect,[19] such that electrons can accumulate in the acceptor region ready for injection into the TiO_2 film. Efficient ICT from the HOMO localized donor moiety to the LUMO localized acceptor moiety in a dye also correlates with enhanced light absorption and a smaller HOMO−LUMO gap (E_g).[20,21]

Azo dyes are a well-known family of organic dyes with their defining −N=N− group, often connecting two arene rings (Scheme 1). They are versatile materials, already being widely used in the textile, painting, and printing industries owing to their easy synthesis, sublimation fastness, light-fastness, and presentation of a large variety of vivid colors.[22−26] However, only a handful of studies[27,28] have demonstrated the successful

Received: June 17, 2013
Revised: August 20, 2013
Published: August 27, 2013

Scheme 1. Schematic Chemical Structure of 1−7[a]

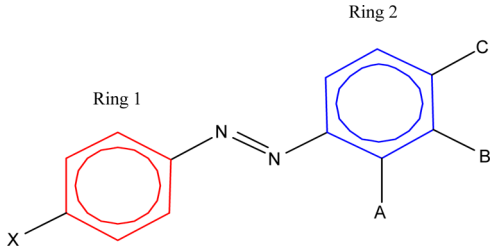

[a]Ring 1 and ring 2 are colored red and blue, respectively. **1**: *X* = $N(CH_3)_2$, *A* = COOH, *B* = H, *C* = H. **2**: *X* = $N(C_2H_5)_2$, *A* = COOH, *B* = H, *C* = H. **3**: *X* = $N(C_3H_7)_2$, *A* = COOH, *B* = H, *C* = H. **4**: *X* = $N(CH_3)_2$, *A* = H, *B* = H, *C* = COOH. **5**: *X* = $N(C_2H_5)_2$, *A* = H, *B* = H, *C* = COOH. **6**: *X* = $N(C_3H_7)_2$, *A* = H, *B* = H, *C* = COOH. **7**: *X* = $N(CH_3)_2$, *A* = H, *B* = COOH, *C* = H.

incorporation of azo dyes into DSSCs, and few have analyzed them in terms of relating their molecular structure to DSSC properties. Similar molecules such as nitroazobenzene compounds have been demonstrated in optoelectronic applications, being effective in electro-optical devices, most famously exemplified by the Disperse Red 1 azo dye.[29,30]

The anchoring groups, which enable adsorption of the dye onto the TiO_2 nanoparticles for electron injection, have been studied by various groups.[31−34] The carboxylic acid group is, by far, the most common anchoring group, although alternative options such as $-SO_3H$, $-H_2PO_3$, hydroxyl, pyridine, and hydroxamate groups have been developed.[17,35−37] Although most dyes are designed in such a way that the anchoring group is at the *para*-position, there is a lack of systematic studies to seek their molecular origin. There are several papers discussing anchoring position effect in porphyrin dyes.[31,38,39] Because of the significant structural differences between porphyrin dyes and most organic dyes including azo dyes, the anchoring effects of these azo dyes, in combination with donor effects, will be discussed in detail employing various spectroscopic and related techniques. In this paper, seven aminoazobenzene dyes with varying electron donating groups and carboxylic acid anchoring moieties (Scheme 1) are investigated: (**1**) 2-[2-[4-(dimethylamino)phenyl]diazenyl]-benzoic acid; (**2**) 2-[2-[4-(diethylamino)phenyl]diazenyl]-benzoic acid; (**3**) 2-[2-[4-(dipropylamino)phenyl]diazenyl]-benzoic acid; (**4**) 4-[2-[4- (dimethylamino)phenyl]diazenyl]-benzoic acid; (**5**) 4-[2-[4-(diethyl-amino)phenyl]diazenyl]-benzoic acid; (**6**) 4-[2-[4-(dipropylamino)phenyl]diazenyl]-benzoic acid; and (**7**) 3-[2-[4-(dimethylamino)phenyl]diazenyl]-benzoic acid. These seven azo dyes can be split into three distinct groups: **1**−**3**, which have the anchoring carboxylic acid group at the *ortho*-position on Ring 2 (Scheme 1) relative to the azo group, referred to hereafter as "*ortho*- dyes"; **4**−**6**, in which the anchoring group is at the *para*-position, referred to hereafter as "*para*-dyes"; and **7**, in which the anchoring group is at the *meta*-position. Herein, we report the synthesis of azo dyes based on the traditional azo coupling method[40] and the crystal structures of **1**−**4** and two polymorphs of **5** (**5a** and **5b**). UV/vis absorption and ^{1}H NMR spectroscopy, along with density functional theory calculations, are employed to examine and rationalize the relationship between the molecular structures and photovoltaic properties of these azo dyes. To this end, fabrication and operational performance testing of liquid-based single-layer dye-sensitized solar cells were also performed.

EXPERIMENTAL AND COMPUTATIONAL METHODS

Materials and Synthesis. **1**, **2**, and **3** were supplied by Sigma Aldrich, while **4** and **7** were purchased from TCI and used without further purification. The synthesis and crystallization of **5** and **6** were conducted following literature methods.[41] Crystals of **1**, **2**, and **3** suitable for X-ray crystallography were grown via slow solvent evaporation in methanol at room temperature, while the crystal of **4** is grown in pyridine.

Preparation of **5**. 4-Aminobenzoic acid (1.65 g, 12 mmol) was dissolved in ethanol (20 mL) with 2 mL of acetic acid. Sodium nitrite (1 g, 14 mmol) in 2 mL of water was added to this mixture. After vigorous stirring in an ice bath for 30 min, the resulting suspension was neutralized with sodium carbonate. Leaving the reaction mixture overnight yielded crystals of the first polymorph of **5** (**5a**, yield: 50%).

Table 1. Experimental Single-Crystal X-ray Diffraction and Structural Refinement Details for the 120 K Crystal Structures of 1−3, 5a, and 5b

	1	2	3	4	5a	5b
chemical formula	$C_{15}H_{15}N_3O_2$	$C_{17}H_{19}N_3O_2$	$C_{19}H_{23}N_3O_2$	$C_{15}H_{15}N_3O_2$	$C_{17}H_{19}N_3O_2$	$C_{17}H_{19}N_3O_2$
Mr	269.3	297.35	325.4	269.3	297.35	297.35
crystal system	triclinic	monoclinic	monoclinic	monoclinic	monoclinic	triclinic
space group	*P*-1	$P2_1/c$	$P2_1/n$	$P2_1/c$	$P2_1/c$	*P*-1
a (Å)	8.252 (5)	10.529 (4)	10.214 (6)	16.072 (4)	12.241 (5)	7.921 (5)
b (Å)	8.511 (5)	17.052 (6)	13.482 (8)	7.3250 (19)	8.264 (3)	14.169 (10)
c (Å)	11.230 (7)	8.348 (3)	12.661 (7)	14.970 (4)	15.473 (6)	14.875 (11)
α (deg)	92.512 (4)	90	90	90	90	110.092 (8)
β (deg)	110.205 (8)	92.743 (4)	98.953 (1)	91.207 (4)	100.650 (5)	103.584 (9)
γ (deg)	113.719 (4)	90	90	90	90	90.916 (5)
V (Å^3)	662.1 (7)	1497.1 (9)	1722.2 (17)	1762.0 (7)	1538.3 (10)	1515.4 (18)
Z	2	4	4	4	4	4
crystal size (mm)	0.25, 0.15, 0.09	0.30, 0.18, 0.07	0.17, 0.15, 0.10	0.29, 0.26, 0.20	0.16, 0.13, 0.11	0.41, 0.24, 0.22
μ (Mo Kα) (mm^{-1})	0.71073	0.71073	0.71073	0.71073	0.71073	0.71073
D_c (Mg m^{-3})	1.351	1.319	1.255	1.313	1.284	1.303
total reflections	5525	7209	8009	14056	10190	12397
independent reflections (R_{int})	3012 (0.0424)	3397 (0.0529)	3904 (0.0548)	4032 (0.0794)	2694 (0.0406)	6835 (0.0432)
T_{min}, T_{max}	0.861, 1	0.602,1	0.842, 1	0.843, 1	0.864, 1	0.838, 1
final *R*, wR_2	0.0476, 0.1390	0.0538, 0.1347	0.0691, 0.1485	0.0593, 0.1601	0.0630, 0.1668	0.0685, 0.1813
$\Delta\rho_{max}$, $\Delta\rho_{min}$ (e Å^{-3})	0.248, −0.197	0.286, −0.233	0.255, −0.180	0.312, −0.257	0.674, −0.292	0.490, −0.408

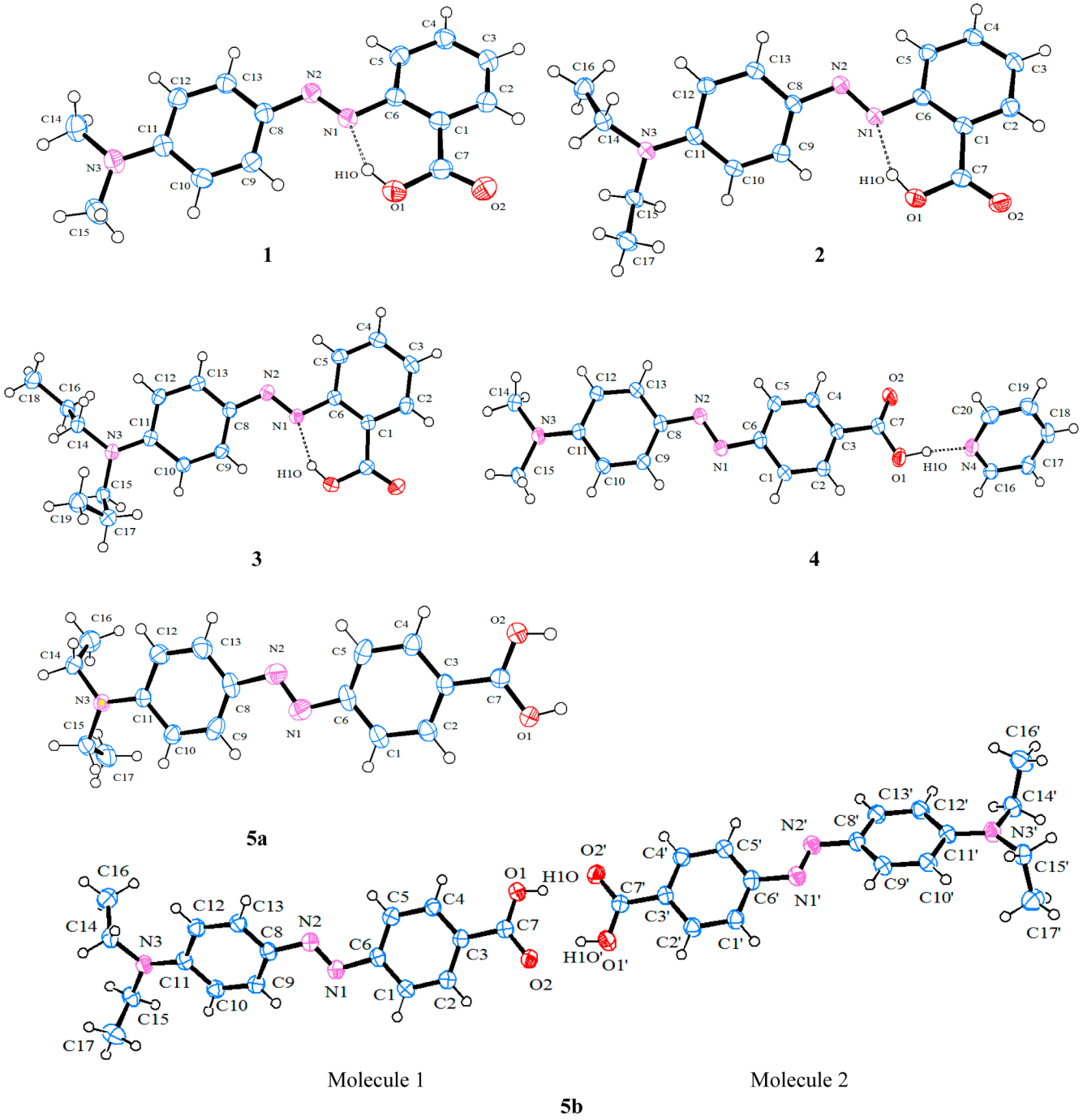

Figure 1. Structures of **1**, **2**, **3**, **4**, **5a**, and **5b** with atomic displacement ellipsoids drawn at the 50% probability level. Intramolecular hydrogen bonds are shown by dashed lines. **4** crystallizes as a pyridine solvate. Disorder exists in the carboxylic acid group of **5a**.

Crystals of a second polymorph (**5b**) were grown via slow evaporation of the solvent from a solution of **5** in ethanol.

Preparation of ***6****.* 4-Aminobenzoic acid (1.65 g, 12 mmol) was dissolved in 20 mL of ethanol including 2 mL of acetic acid. Sodium nitrite (1 g, 14 mmol) followed by *N*,*N*-dipropylaniline (2 mL, 12.5 mmol) was added to this solution. The resulting suspension was neutralized with sodium carbonate (yield: 50%).

Single-Crystal X-ray Diffraction. Crystal structure data were collected for **1**−**4**, **5a**, and **5b** (Table 1, Figure 1) at 120 K on a Rigaku Saturn 724+CCD diffractometer equipped with a Mo Kα X-ray generator ($\lambda_{MoK\alpha}$ = 0.71073 Å) and an Oxford Cryosystem CryostreamPlus. Rigaku *CrystalClear*-SM Expert 2.0 software[42] using ABSCOR[43] for the absorption correction was used for data collection and reduction. WinGX 1.80.05[44] implemented with SHELXL-97[45] was used to solve and refine all crystal structures. CCDC 935172−935176 contains supplementary crystallographic data for this paper.

Dye **4** crystallizes as a pyridine solvate, forming an intermolecular hydrogen bond between the acid group and the nitrogen atom of pyridine molecule, rather than forming a dimer between two carboxylic acid groups. Though the hydrogen-bonding environment is different in this case, the presence of the pyridine molecule does not impact upon the bond geometry, and hence, this solvate was considered appropriate for bond length pattern analyses.

It should be noted that room temperature or other higher temperature determinations of **1** and **2** have been reported previously.[46] However for this study, it was important to collect all structural data at low temperature (120 K) in order to reduce atomic thermal vibrations

Table 2. List of Selected Bond Lengths (Å) for 1−4, 5a, and 5b Compared with Typical Bond Lengths from the International Tables for Crystallography[60]

		ortho-dyes			*para*-dyes				
bond type	bond	1	2	3	4	5a	5b		typical bond length
							molecule 1	molecule 2	
N_{azo}−N_{azo}	N1−N2	1.2766 (17)	1.2745 (19)	1.281 (2)	1.2653 (17)	1.242 (3)	1.265 (2)	1.268 (2)	1.255
C_{ar}−N_{azo}	C6−N1	1.4205 (18)	1.4212 (19)	1.421 (3)	1.4277 (18)	1.449 (3)	1.430 (2)	1.426 (2)	1.431
	C8−N2	1.3878 (18)	1.396 (2)	1.394 (3)	1.4065 (18)	1.440 (3)	1.411 (2)	1.416 (2)	1.431
C_{ar}−C_{ar}	C1−C2	1.396 (2)	1.395 (2)	1.392 (2)	1.388(2)	1.381 (3)	1.387 (3)	1.383 (3)	1.384
	C2−C3	1.389 (2)	1.388 (2)	1.378 (3)	1.395(2)	1.395 (3)	1.395 (3)	1.398 (3)	1.384
	C4−C5	1.378 (2)	1.385 (2)	1.380 (3)	1.387(2)	1.393 (3)	1.392 (3)	1.392 (3)	1.384
	C9−C10	1.371 (2)	1.371 (2)	1.371 (3)	1.373(2)	1.389 (3)	1.375 (3)	1.379 (3)	1.384
	C12−C13	1.371 (2)	1.374 (2)	1.376 (3)	1.3777(19)	1.373 (3)	1.378 (3)	1.382 (3)	1.384
C_{ar}−COOH	C1−C7	1.5095 (19)	1.511 (2)	1.506 (3)	–	–	–	–	1.484
	C3−C7	–	–	–	1.4946(19)	1.476 (3)	1.477 (3)	1.472 (2)	1.484

Table 3. Selected Interplanar Angles (deg) for 1−4, 5a, and 5b

	ortho-dyes			*para*-dyes			
	1	2	3	4	5a	5b	
						molecule 1	molecule 2
ring 1−ring 2	13.06 (9)	39.90 (6)	6.36 (12)	3.78 (8)	4.98 (13)	38.29 (8)	25.74 (9)
ring 1−azo	6.29 (20)	14.11 (14)	4.38 (26)	4.22 (17)	3.18 (0.27)	9.39 (0.21)	10.92 (0.20)
ring 2−azo	4.92 (20)	23.92 (11)	1.02 (25)	7.84 (16)	5.78 (0.24)	27.59 (0.11)	15.49 (0.20)
RMS deviation	0.1462	0.4125	0.1273	0.0826	0.0719	0.3399	0.2280

and to ensure internal consistency of results for the purposes of reliable structural comparisons.

DSSC Fabrication and Performance Testing. TiO_2 paste (DSL 18NR-T) and FTO-coated glass (TEC15) were purchased from Dyesol. A single TiO_2 layer was deposited onto the FTO glass via the doctor-blade method; sensitization was achieved using a 0.5 mM solution of dye in 1:1 acetonitrile:tert-butanol solvent. The platinum counter-electrodes were prepared via the same doctor-blade method using chloroplatinic acid hexahydrate ($H_2PtCl_6{\cdot}6H_2O$) from Sigma, diluted to 52 mM with isopropanol. Each cell was sealed with a 25 μm thick film of Surlyn separating the two electrodes, with an electrolyte, consisting of a 50 mM iodide/tri-iodide redox couple in acetonitrile solution injected in between them. At least five duplicate cells for each dye were made and tested in order to ensure consistency of DSSC results (Table S3, Supporting Information). The incident-photon-to-current-efficiency (IPCE) was quantified by illuminating the DSSC with a spectrally resolved halogen lamp, as calibrated by a silicon diode. Current−voltage (*J*-*V*) characteristic responses and overall DSSC efficiencies were determined using an ABET Sun 2000 solar simulator under AM1.5 illumination at 100 mW cm^{-2}.

^{1}H NMR and UV/vis Absorption Spectroscopy. UV/vis absorption spectra of all dyes in solution were obtained using an Agilent8453 diode array spectrophotometer. A Bruker Avance 500 CryoUltrasheld NMR spectrometer was used for ^{1}H NMR spectroscopy on **1**, **4**, and **7** dissolved in deuterated DMSO. Temperature coefficients were determined from chemical shifts at five temperatures: 298, 303, 308, 313, and 318 K.

Density Functional Theory and Time-Dependent Density Functional Theory. All calculations were carried out using Gaussian 09[47] and visualized using Gaussview. Structural optimizations and subsequent frequency calculations for the ground state were performed by DFT using a B3LYP functional[48] and 6-31+g(d,p) basis set[49] in vacuo initially. Theoretical UV/vis absorption spectra were computed via TDDFT using B3LYP,[48] PBE1PBE,[50] BMK,[51] and M06-2X[52] functionals and pure Hartree−Fock (HF) theory. Solvent effects were then included using the popular integral equation formalism polarisable continuum model (IEFPCM)[53] in DMSO solvent to determine absorption spectra and HOMO−LUMO levels. The self-consistent isodensity polarized continuum model (SCIPCM),[54] which includes effects of solvation in iterative self-consistent field computation, was also employed at the B3LYP level. For intramolecular hydrogen bond (HB) characterization and HOSE model calculations in solution, DFT with B3LYP/6-31+g(d,p) in DMSO was employed using IEFPCM.

RESULTS AND DISCUSSION

Intramolecular Charge Transfer. *Crystal Structures.* The single-crystal X-ray structures solved and refined for **1**−**5** (Figure 1) can be analyzed in terms of molecular geometry (Table 2) in order to further understanding of the charge-transfer processes that govern their suitability for DSSCs. Alignment of the π-system is important in order to ensure low-energy charge separation. The level of such alignment can be quantified by considering the ring-to-ring and ring-to-azo group interplanar angles within the molecule (Table 3) because the relative alignment of these moieties largely dictates the overall level of molecular planarity; the closer their alignment, the greater the level of π-overlap that renders lower energy ICT. To enumerate the overall level of molecular planarity, the root-mean-square (RMS) deviation of all non-hydrogen atoms from the plane defined by all non-hydrogen atoms, except the carbon atoms in alkyl chains, was calculated. Relatively low RMS deviations (<0.15 Å) and ring-to-ring and ring-to-azo group angles ($\lesssim$13°) were observed, except in the cases of **2** and **5b**.

Considering the two polymorphs of **5** determined in this study, the ethyl chains of the amino group in **5a** are both on the same side of the molecular plane, while they are located on opposite sides of the molecular plane in **5b**. The crystal packing of these two polymorphs is dramatically different. This is manifest in the differing crystal systems and space groups observed in each structure; **5a** is monoclinic and adopts the space group $P2_1/c$, while **5b** is triclinic and adopts the space group *P*-1. In terms of conformational variation between the two polymorphs, **5a** exhibits a smaller angle between the two

phenyl rings, which is reflected by its lower RMS deviation value than that in **5b**. DFT calculations indicate that **5b** possesses a lower total energy in **5b** (0.37 eV less than **5a**); indeed the solvent evaporation process during crystallization is much slower for **5b** than that of **5a**. As a result, the more stable polymorph **5b** will be used for the discussion of ICT and related mechanisms in this paper.

One of the most striking attributes of the *ortho*-dye crystal structures is their lack of intermolecular hydrogen bonds despite the presence of a carboxylic acid group. Instead, an intramolecular hydrogen bond is formed owing to the *ortho*-position of the acid group in **1**−**3** (Figure 1); the acid proton acts as a donor to the N1 in the azo group to form a pseudo-six-membered ring classified by the hydrogen-bonding graph set, $S(6)$.[55] The presence of this intramolecular hydrogen bond is not unexpected, as it is predicted by Etter's second rule;[56] however, it is an important consideration where DSSC applications are of concern because this intramolecular hydrogen bond affects the photostability of dyes[57] and may prove to be a hindrance to the ability of the dye to anchor onto a TiO_2 surface (vide infra).

Structure−Property Relationships Explained by Resonance Theory. Potential intramolecular charge transfer pathways in these dyes can be derived using resonance theory,[58,59] which identifies possible resonance structures. By comparing these structures to single-crystal X-ray diffraction structural data, we can examine the dominant ICT pathways in these dyes. The three most probable resonance structures of these azo dyes are shown in Figure 2, in which three canonical forms (Q, K1, and K2) are highlighted.

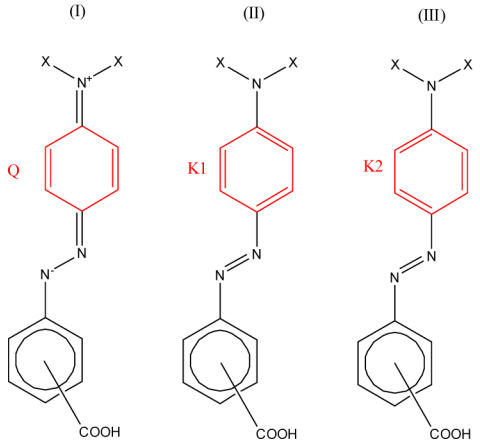

Figure 2. Three possible resonance structures (I), (II), and (III) in the azo dyes. The red-highlighted ring 1 moieties represent three canonical molecular fragments: Q, K1, and K2. Q is the quinoidal structure. K1 is Kekulé configuration 1. K2 is Kekulé configuration 2.

The effects of the ICT predicted by resonance theory are manifested in the bond length patterns observed in the azo dye molecules (Table 2). The azo (N1−N2) bond in all structures, with the exception of **5a**, is observed to be longer than that of typical $C_{ar}-N{=}N-C_{ar}$ bonds (1.255(16) Å).[60] This elongation is presumably due to a predominance of resonance structure (I) where N1−N2 is represented by a single bond. In addition, considering the neighboring $N_{azo}-C_{ar}$ bond lengths, N1−C6 and N2−C8 (Table 2), the contribution of resonance structure (I) is clear. Both of these two bonds are shorter than the typical $N_{azo}-C_{ar}$ bond length value [1.431(20) Å][60] for all of the crystallographically determined azo dyes except the less stable **5a**. For example, N2−C8, which connects ring 1 to the azo group, is 0.015−0.043 Å smaller than the typical $N_{azo}-C_{ar}$ bond length value. The $N_{amino}-C_{benzenoid}$ N3−C11 bond length is another indicator of quinoidal structure in ring 1; indeed, N3−C11 is distinctly (0.07−0.08 Å) shorter (Table S1 and S2, Supporting Information) than the reference $N_{amino}-C_{benzenoid}$ bond length (1.431 Å) in all of the subject dyes.

In both *ortho*- and *para*-dyes, the significant contribution of *para*-quinoidal resonance to ring 1 can be observed via the shortening of bonds C9−C10 and C12−C13 relative to the other bonds in the benzene ring, except for **5a**; see Table 3 versus the International Tables for Crystallography reference values for an aromatic bond in a benzene ring (1.384 Å).[61] Previous studies have linked this *para*-quinoidal character to ICT and optoelectronic properties.[62,63]

It is possible to quantify the relative contribution of these resonance forms via harmonic oscillator stabilization energy (HOSE) calculations

$$\mathrm{HOSE} = \frac{1}{2}\left[\sum_{r=1}^{n_1}(R_r' - R_o^s)^2 k_r' + \sum_{r=1}^{n_2}(R_r' - R_o^d)^2 k_r''\right] \quad (1)$$

where k_r' and k_r' are defined by

$$k_r' = a + bR_r'; \qquad k_r'' = a + bR_r'' \quad (2)$$

For carbon−carbon bonds, R_o^s = 1.467 Å, R_o^d = 1.349 Å, a = 44.39 × 10^4 Pa, and b = −26.02 × 10^4 Pa/Å, so eq 1 could be represented as

$$\mathrm{HOSE} = 301.15\left[\sum_{r=1}^{n_1}(R_r' - 1.467)^2(44.39 - 26.02R_r') + \sum_{r=1}^{n_2}(R_r'' - 1.349)^2(44.39 - 26.02R_r'')\right] \quad (3)$$

The relative contributions of different resonance states are calculated by

$$C_i = \frac{(\mathrm{HOSE}_i)^{-1}}{\sum_{j=1}^{N}(\mathrm{HOSE}_j)^{-1}} \quad (4)$$

For each structure, a HOSE calculation was performed on ring 1 and ring 2 in order to assess the relative contributions of Q, K1, and K2 (Figure 2 and Figure S1, Supporting Information). As discussed, HOSE values for **5b** are regarded as a more accurate representation of **5** because this polymorph, as opposed to **5a**, was determined to be the lowest energy from DFT calculations.

Table 4 lists calculated K1, K2, and Q contributions from single-crystal X-ray diffraction, demonstrating that the Q contribution is larger than K1 and K2 in ring 1 of these *para*- and *ortho*-azo dyes. For example, the Q contribution is 0.40 for molecule 1 in **5b**; this indicates high levels of ICT.[64] Ring 2, on the other hand, exhibits a reduced Q contribution probably due to the electron withdrawing nature of the azo group,[65] although Q is generally dominant in ring 2.

HOSE values from DFT in the gas phase and solution phase predict the same trend as the solid-phase experimental data (Table 4). For example, both gas and solution phase models indicate that the Q contribution is dominant in ring 1 for all of these crystallographically determined dyes. This indicates that the ICT predicted by the HOSE model in the solid-state (single-crystal X-ray diffraction) is transferable to the solution phase (DSSC). This is very pertinent to the solution−solid

Table 4. HOSE Values and Relative Contributions of Bond Length Patterns in the Benzene Rings of 1−3, 5a, and 5b

			1			2			3		
			K1	K2	Q	K1	K2	Q	K1	K2	Q
ring 1	experiment	*Ci*	0.25	0.23	0.52	0.27	0.24	0.48	0.28	0.21	0.52
	DFT gas	*Ci*	0.28	0.24	0.48	0.28	0.24	0.49	0.27	0.24	0.49
	DFT solution	*Ci*	0.23	0.21	0.56	0.23	0.20	0.57	0.23	0.20	0.57
ring 2	experiment	*Ci*	0.30	0.33	0.37	0.32	0.33	0.35	0.27	0.39	0.34
	DFT gas	*Ci*	0.29	0.33	0.38	0.29	0.33	0.38	0.29	0.33	0.38
	DFT solution	*Ci*	0.28	0.33	0.38	0.29	0.33	0.39	0.29	0.33	0.39

			4			5a			5b					
									molecule 1			molecule 2		
			K1	K2	Q	K1	K2	Q	K1	K2	Q	K1	K2	Q
ring 1	experiment	*Ci*	0.31	0.25	0.44	0.31	0.31	0.38	0.33	0.28	0.40	0.35	0.27	0.38
	DFT gas	*Ci*	0.32	0.27	0.41	0.29	0.25	0.46	0.29	0.25	0.46	0.29	0.25	0.46
	DFT solution	*Ci*	0.30	0.26	0.44	0.26	0.22	0.52	0.26	0.22	0.52	0.26	0.22	0.52
ring 2	experiment	*Ci*	0.30	0.35	0.35	0.32	0.34	0.34	0.32	0.37	0.31	0.35	0.31	0.34
	DFT gas	*Ci*	0.29	0.34	0.37	0.29	0.34	0.37	0.29	0.33	0.37	0.30	0.33	0.37
	DFT solution	*Ci*	0.29	0.33	0.38	0.29	0.33	0.38	0.29	0.33	0.38	0.28	0.36	0.36

interface that governs azo dye photovoltaic performance in DSSC applications; one can therefore conclude from these ICT findings alone that these dyes afford good intrinsic potential for DSSC application.

Optical Band Gap Characteristics of ICT. A qualitative representation of ICT can be given by HOMO and LUMO plots, as shown for these dyes in Figure 3, in which the effect of solvent was included in the calculation. ICT will be facilitated if the HOMO and LUMO are separated by electronic push−pull effects; in other words, it is ideal for the HOMO electron-density distribution to be located near to the electron donor, while that of the LUMO is distributed around an anchoring group, ready for electron injection into the conduction band of the TiO_2 semiconductor.[66−69]

Figure 4 compares the HOMO−LUMO energy levels of the azo dyes. All dyes have higher LUMO energy levels than that of the base level of the TiO_2 conduction band (−4.04 eV)[70] and lower HOMO energy levels than that of the most commonly employed I^-/I_3^- electrolyte redox level (−4.94 eV);[70] these findings, respectively demonstrate their viability to undergo electron injection and dye regeneration within a DSSC. The *para*-dyes except for **6** have higher LUMO energy levels for electron injection compared with their *ortho*-dye counterparts. The HOMO and LUMO levels of **6** are likely underestimated; it has the longest molecular axis due to the propyl group and *para*-COOH-anchoring position and the standard B3LYP functional struggles in the case of long-range.[71] Dye **7** presents a large band gap (3.28 eV) owing to its *meta*-COOH substitution; this corresponds to an absorption wavelength of 378 nm, i.e., the tail end of the solar spectrum, leaving this dye in difficulty to realize significant light absorption to generate an excited state upon solar irradiation.

Intramolecular Hydrogen Bonding in Solution. *Density Functional Theory Calculations.* An intramolecular HB is observed in all *ortho*-substituted azo dyes in the solid state (Table 5). Its level of retention through to the solution state was important to assess. From an applied perspective, such an HB stands to influence the photostability of dyes and the anchoring ability of the dye to the TiO_2 in a DSSC, while the dye exists in solute within this operational cell; querying such HB retention is particularly pertinent because all molecules can display much higher conformational flexibility in solution.

In order to confirm intramolecular hydrogen bonding in the solution state, DFT was first employed in order to calculate the energy of the three different molecular configurations of **1** (Scheme 2). "Intra" is defined here as the configuration containing an intramolecular HB, while "Inter1" and "Inter2" represent two forms of intramolecular HB dissociation that affords an intermolecular HB with neighboring solvent. An extra DMSO molecule is included in the DFT modeling in order to consider the local interaction between the dye and solvent molecules.

Table 6 shows that although Inter1 has the lowest electronic energy, the energy barrier between Inter1 and Intra is only 0.0016 hartree (∼0.04 eV), i.e., comparable to thermal energy at room temperature (0.039 eV). On the basis of DFT, the coexistence of intramolecular and intermolecular hydrogen bonding with solvent in DMSO solution is therefore predicted.

Solution ^{1}H NMR Spectroscopy. Intramolecular HBs play important roles in the photochemical stability of organic dyes.[57] In order to substantiate these calculations by experiment, ^{1}H NMR spectroscopy was employed; this is a reliable tool by which one can examine intramolecular hydrogen bonding in solution.[72−75]

Dyes **1**, **4**, and **7** were selected for ^{1}H NMR experiments as the exemplars of *ortho*-, *para*-, and *meta*-carboxylic acid anchoring groups, respectively. Hydrogen atoms participating in intramolecular hydrogen bonding typically exhibit larger chemical shifts and smaller temperature coefficients in their ^{1}H NMR spectra.[76,77] The carboxylic acid proton of **1** was indeed found to exhibit a larger chemical shift than that of **4** (Figure 5), which is not capable of forming an intramolecular HB. This result suggests that the intramolecular HB in **1** is still present in solution. In addition, the chemical shift in **1** has a smaller temperature coefficient (4.8 ppm/K) than that of **4** and **7** (6.0 and 6.1 ppm/K, respectively). These two factors do suggest retention of the intramolecular hydrogen bond in solution. However, the temperature coefficient of the acidic proton in **1** is slightly larger than that of other compounds solely exhibiting intramolecular hydrogen bonding (ca. 1−3 ppb/K).[77] Its chemical shift is also similar to that of **4** and **7**, which are incapable of forming an intramolecular HB. All of these observations can be made consistent by reasoning that for *ortho*-dyes the intramolecular HB coexists with other forms of hydrogen

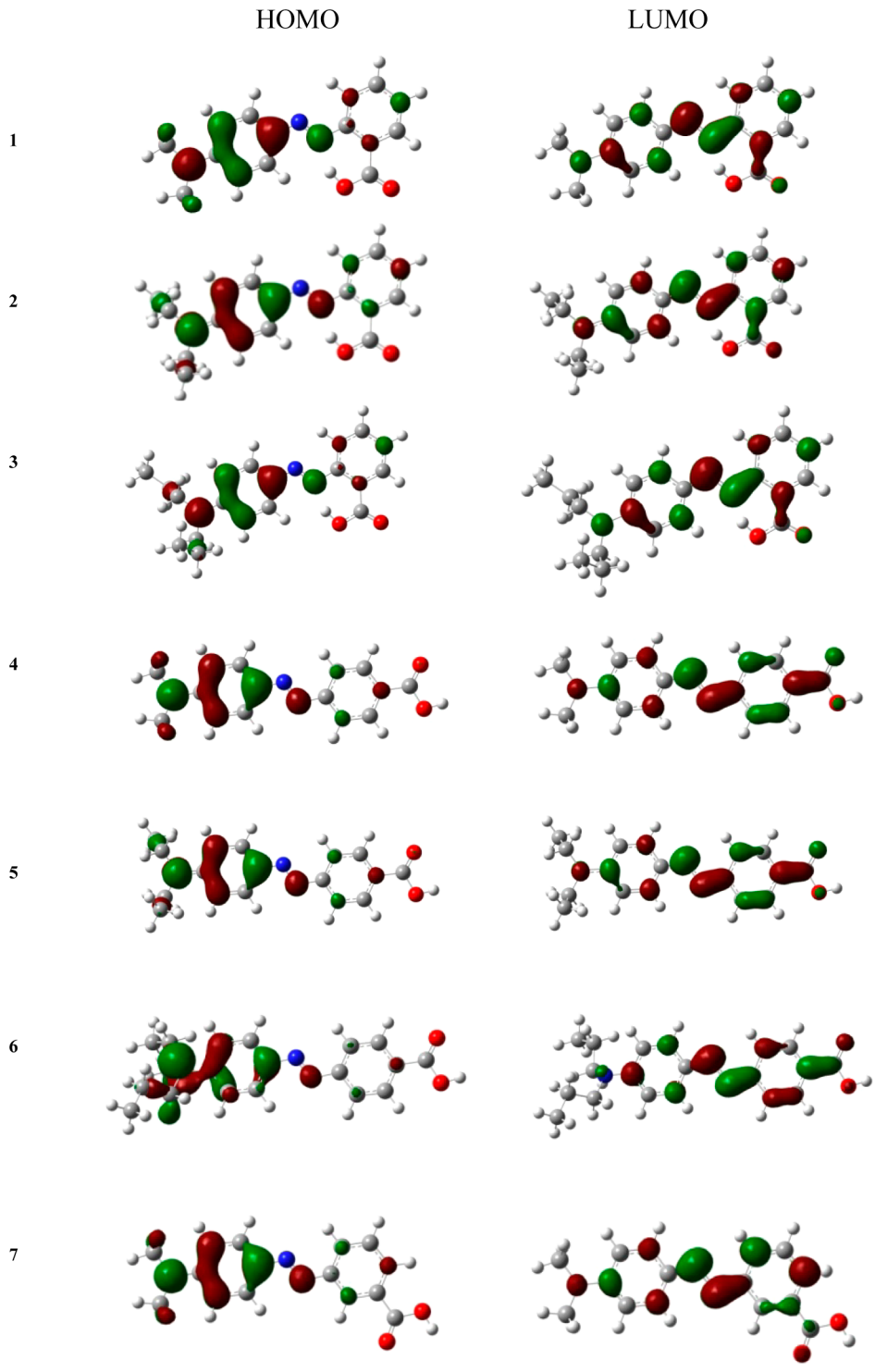

Figure 3. HOMO−LUMO visualization of azo dyes **1**−**7**.

bonding, such as intermolecular hydrogen bonding with solvent molecules.

When the carboxylic acid group lies at the *meta*- or *para*-position, such as in **5a**, **5b**, and **7** (Figure 1), it is unlikely to form an intramolecular HB. Hence, the acid proton is free to engage in intermolecular hydrogen bonding. Indeed both **5a** and **5b** form closed dimers in the solid state via intermolecular hydrogen bonding between two carboxylic acid moieties; the resulting ring motif is classified by the graph set $R_2^2(8)$.[55] The dimer in **5a** forms about a crystallographic center of inversion via O1−H1···O2 interactions (symmetry operator: $1 - x, - y, - z$), whereas the dimer in **5b** comprises two crystallographically independent molecules. Again, the behavior of the carboxylic acid has a significant impact on its role as the anchoring group in dye molecules used in DSSC applications. The *para*-positioning of the acid group suggests that it would be free to bind to TiO_2 more readily than where acid groups are bound by an intramolecular HB, e.g., in **1**−**3**.

These joint computational and experimental studies confirm the presence of both inter- and intramolecular HBs in the structure of

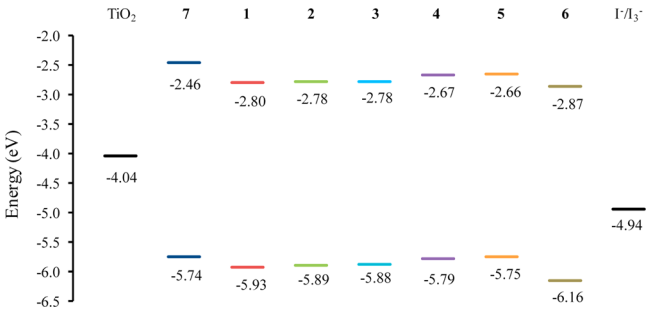

Figure 4. HOMO−LUMO energy levels of azo dyes compared with the bottom of the TiO_2 conduction band and the redox potential of the most commonly employed electrolyte, I^-/I_3^-.[70]

Table 5. Intramolecular Hydrogen Bond Geometry (Å, deg) for 1−3

	D−H···*A*	*D*−H	H···*A*	*D*···*A*	*D*−H···*A*
1	O1−H1O···N1	0.95	1.70	2.588	153
2	O1−H1O···N1	0.92	1.73	2.575	153
3	O1−H1O···N1	0.93	1.74	2.581	151

the *ortho*-dyes. Considering the possible likely bonding mechanisms of organic molecules adsorbing onto TiO_2, bidentate modes involving the −COOH group have already been identified as the most energetically favorable states.[78−80] However, the hydroxyl oxygen and hydrogen atoms in intramolecular hydrogen bonding are stable in the pseudo-six-membered ring that the HB creates, such that the −COOH anchoring group is in an unfavorable geometry and energy state to attach onto the TiO_2 surface; in turn, this will inhibit the formation of a bidentate mode. In addition, the hydrogen in the −COOH group is demonstrated to stabilize anchoring onto TiO_2;[78] however, in this case the intramolecular HB prevents the hydrogen atom from stabilizing the adsorption of the organic molecule onto TiO_2.

Solution-Based UV/Vis Absorption Spectra. Figure 6 shows UV/vis absorption spectra of azo dyes **1**−**7** in DMSO (0.05 mM), and Table 7 lists their corresponding absorption peaks. Solubility

Table 6. Energy Calculated by DFT for 1 with Different Molecular Configuration as in Scheme 2

	Intra	Inter1	Inter2
sum of electronic and zero-point energies (Hartree)	−1448.249	−1448.251	−1448.239
ΔE (Hartree)	0	−0.002	0.010
ΔE (eV)	0	−0.04	0.27

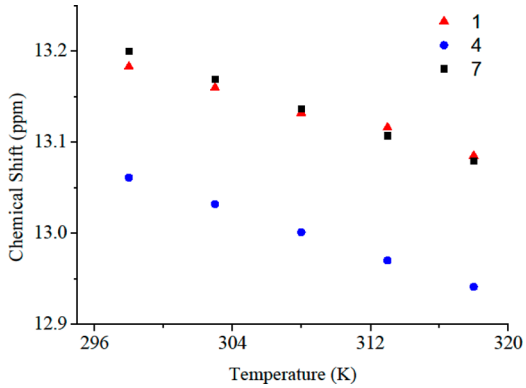

Figure 5. Solution ^{1}H NMR chemical shifts of **1**, **4**, and **7** as a function of temperature.

of these azo dyes, especially *para*-dyes, in DMSO is much better compared with their dissolution in many other solvents such as acetonitrile. As a result, dye aggregation effects, to which planar molecules are prone, are kept to a minimum when DMSO is selected.

Para-dyes are 15−23 nm red-shifted in comparison to the *ortho*-dyes; for example, **1** shows a peak at 432 nm, while **4** is red-shifted to 449 nm. The reason for this is that ICT along the long axis of the molecule produces a red-shift in absorption more effectively than ICT along a short axis.[64]

A monotonic red-shift is observed when a donor is changed from a dimethylamino to diethylamino to dipropylamino group. As the number of carbon atoms increases in the donor, the

Scheme 2. Three Possible Hydrogen-Bonding Configurations of 1

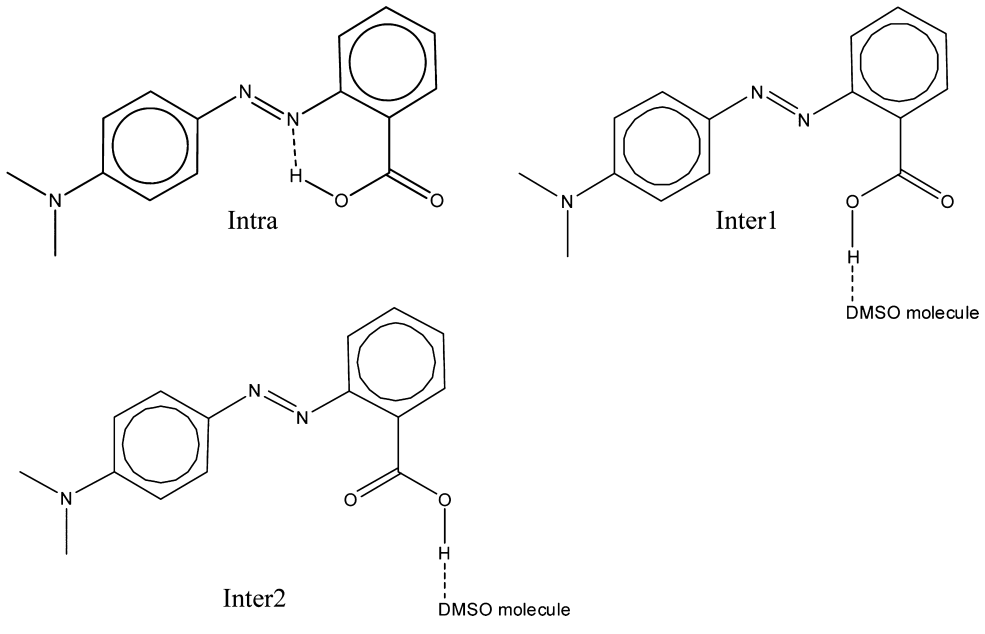

dx.doi.org/10.1021/sc400183t | ACS Sustainable Chem. Eng. 2013, 1, 1440−1452

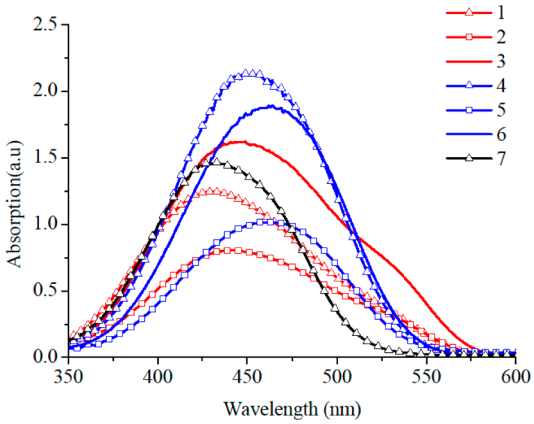

Figure 6. Experimental UV/vis absorption spectra of seven azo dyes in DMSO at 0.05 mM concentration.

Hammett value will also increase leading to a stronger electron donating ability;[81] as a result, ICT is facilitated. Although **7** possesses a longer molecular axis for ICT than **1**, both experiments and calculations agree that its UV/vis absorption is not obviously red-shifted when compared to that of **1**. This is due to the fact that *ortho*-dyes have resonance structures, indicating ICT, while *meta*-dyes inherently lack such resonance.[63]

UV/vis absorption intensity also provides additional information about the molecular structure. The UV/vis absorption peak intensities show the trend: *ortho-* < *meta-* < *para-*. For example, **1** (*ortho-*), **7** (*meta-*), and **4** (*para-*) have absorption intensities of 1.25, 1.46, and 2.13 au, respectively. This indicates better molecular orbital overlap between ground state and excited state[82] for *para*-dyes. In terms of donor effects, the diethylamino group, which induces large angles between two phenyl rings in the crystal structure, coincidentally suppresses absorption intensity in both *ortho-* and *para*-dyes.

Table 7 lists TDDFT results on UV/vis absorption peak positions for the seven dyes, using different hybrid functionals (including pure Hartree−Fock (HF) for comparison) and solvent models. HF methods can also be thought as a hybrid functional consisting of 0% DFT and 100% HF. As the percentage of HF in the hybrid functional increases [B3LYP (20% HF), PBE1PBE (25% HF), BMK (42% HF), M062X (54% HF), HF (100% HF)], the UV/vis absorption peak moves to the blue region, which is in agreement with Kantchev et al.[83] UV/vis absorption peaks derived via the SCIPCM model also agree well with experimental data, except for **3**, where SCIPCM is prone to convergence failure[84], and **5**, which is overestimated compared with experimental data. In general, it can be concluded from both experiments and calculations that UV/vis absorption peak positions for anchoring positions are *para-* > *ortho-* > *meta-*; while ICT for donors is reflected by the trend in peak absorption position as dipropylamino > diethylamino > dimethylamino.

Dye-Sensitized Solar Cell Operational Performance. The *J-V* curves of *ortho-*, *para-*, and *meta*-dyes are shown in Figure 7,

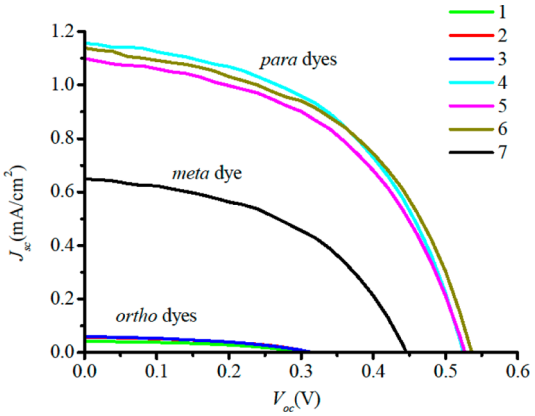

Figure 7. Typical *J-V* curves of solar cells with azo dyes **1**−**7**.

and the corresponding operational performance (overall efficiency η, open circuit voltage V_{oc}, short circuit current density J_{sc}, and fill factor FF) are summarized in Table 8. For comparison purposes,

Table 8. Photovoltaic Performance Based on 1−7

	J_{sc}	V_{oc}	FF	η
N3	11.98	0.67	0.45	3.63
1	0.04	0.30	0.44	0.01
2	0.06	0.31	0.42	0.01
3	0.06	0.32	0.43	0.01
4	1.30	0.54	0.52	0.30
5	1.09	0.52	0.50	0.29
6	1.21	0.53	0.50	0.32
7	0.65	0.45	0.49	0.14

the reference solar cell incorporating the standard N3 dye using the same fabrication method is also shown. The η values are reproducible within 7% for all the dyes, based on repeated fabrication and tests (see ESI, Table S3, Supporting Information), and these efficiencies are comparable to similar studies on azo dye-based DSSCs where efficiencies range from 0.01− 0.35%.[28] In Figure 7, solar cells containing **1**−**7** are clearly grouped in performance according to their −COOH anchoring position. Solar

Table 7. Experimental and Calculated UV/Vis Absorption Peaks Using B3LYP, PBE1PBE, BMK, and M062X and the Pure HF Method, with IEFPCM and SCIPCM as Solvation Models[a]

		1	**2**	**3**	**4**	**5**	**6**	**7**
experiment	–	432	441	449	449	464	464	433
B3LYP	IEFPCM	467	471	473	475	479	477	454
PBE1PBE	IEFPCM	451	455	457	459	463	453	438
BMK	IEFPCM	429	437	432	426	431	396	405
M062X	IEFPCM	419	423	425	412	417	374	394
HF	IEFPCM	356	357	361	347	351	320	333
B3LYP	SCIPCM	440	447	N.A.	447	542	464	432

[a]SCIPCM for **3** is not included due to the convergence failure of SCIPCM.

cells with *para*-dyes (**4**, **5**, and **6**) exhibit the best efficiencies ($\eta \approx$ 0.30%) among all azo dyes studied. In contrast, DSSCs containing *ortho*-dyes (**1**, **2**, and **3**) afforded only 0.01% efficiency. The *meta*-dye displayed a modest efficiency of η = 0.14%, which is less than half that of the *para*-dyes. This superiority of *para*-dyes is nevertheless underestimated in porphyrin dyes.[39] V_{oc}, J_{sc}, and FF follow the same trend, i.e., they all increase when −COOH is changed from the *ortho*- to *meta*- to *para*-position (Figure S2, Supporting Information). η for these dyes is closely related to J_{sc} as both η and J_{sc} increase about 10-fold from *ortho*-dyes to *meta*-dyes and 2-fold from *meta*-dyes to *para*-dyes.

While the DSSC efficiencies in these azo dye exemplars are not high, their performance trends are nonetheless important. It is obvious that these dyes fall into three categories according to their carboxylic acid anchoring position, which is a crucial factor when considering DSSC dye design. As the number of carbon groups in the donating group increases, there is no commensurate alteration in η values, V_{oc}, J_{sc}, or FF. In fact, the electron-donating abilities are quite similar for methyl, ethyl, and propyl groups, as determined from respective Hammett values.[81] As a result, the nature of alkyl donors in these azo dyes has much less impact on DSSC device performance compared with the −COOH anchoring substitution position.

In common with the *J*-*V* responses, IPCE curves of the seven azo dyes also group into three regions (Figure S3, Supporting Information) according to the positions of the anchoring group. The *para*-dyes have larger and broader IPCE curves compared with *ortho*- and *meta*-dyes. The *ortho*-dyes exhibit almost negligible IPCE in most of the visible region and only become observable in the near-UV region (400−500 nm). The IPCE performance of the dyes follow the order: *para*- > *meta*- > *ortho*-.

Because their dominant Q-contribution to ICT offers good intrinsic electronic potential, the rationalization for *ortho*-dyes exhibiting much lower photovoltaic outputs upon DSSC application appears to be geometric in origin. First, the aforementioned intramolecular HB involving the −COOH group diminishes the possibility of dye···TiO_2 anchoring, as in the *ortho*-dyes discussed previously. Second, *ortho*-dyes will poorly align onto the TiO_2 surface, which is needed in order to ensure effective dye adsorption on TiO_2; the plane of the carboxylic acid group will ideally lie perpendicular to the TiO_2 surface. Given that the −COOH group is, in turn, well aligned to the overall molecular plane of the dye, these *ortho*-dye molecules will tend to occupy much of the TiO_2 surface area (Figure 8).

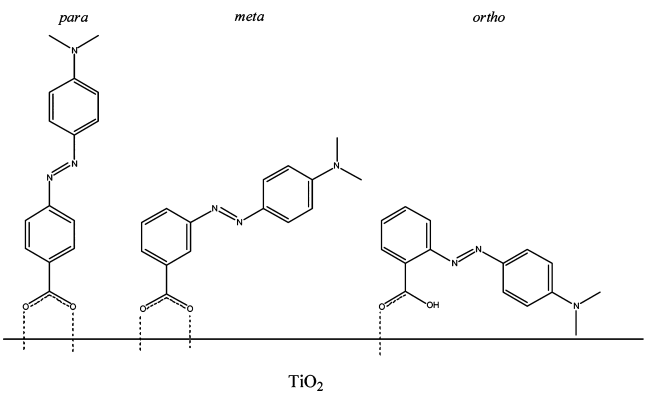

Figure 8. Plausible configurations of *para*-, *meta*-, and *ortho*-azo dyes anchoring to the TiO_2 semiconductor surface.

This will heavily restrict the number of dyes that can be adsorbed onto the TiO_2 semiconductor, thereby compromising the intrinsic DSSC device performance. The case is worsened by progressively increasing steric effects from dimethylamino, diethylamino, and dipropylamino group substitutes on ring 1, as these further hinder the dye contact with the TiO_2 surface. In addition, it has been demonstrated that severe charge recombination occurs when an electron donor is too close to the TiO_2 semiconductor surface.[85,86]

The different amounts of adsorption across the seven azo dyes can be visualized from UV/vis absorption spectra of the dyes as adsorbed onto TiO_2 after the dye sensitization process (Figure S4, Supporting Information). Again, the absorption intensities clearly group into three regions according to the anchoring positions, which is not obvious in the solution-based UV/vis spectra. The UV/vis absorption intensities of azo dyes on TiO_2 nanoparticles follow the order: *para*- > *meta*- > *ortho*-.

The modest DSSC operational performance in the *meta*-azo dye, **7**, relative to the *para*-dyes, can also be rationalized in part by poor alignment of the anchoring group with the TiO_2 surface. Besides, **7** lacks the quinoidal resonance form that benefits *ortho*- and *para*-dyes. It also exhibits a blue-shifted optical absorption peak with respect to that of *para*-dyes, as well as a larger band gap, as determined from its HOMO−LUMO energy difference; as such, its absorption overlaps upon a very weak portion of the solar spectrum, leading to lower DSSC efficiency.

CONCLUSIONS

The molecular structures and optical absorption characteristics of a series of azo dyes have been determined and related to their operational performance when embedded into dye-sensitized solar cell devices. The azo group links to two phenyl moieties, one of which contains a −COOH group that lies *ortho*-, *meta*-, or *para*- to the azo group. The HOSE model from single-crystal X-ray diffraction and DFT predicts the possibility of intramolecular charge transfer for all the azo dyes in gas, solution, and solid phases, demonstrating good intrinsic electronic potential for use in DSSCs. The lack of a resonance quinoidal form and the large optical band gap of the *meta*- dye, **7**, renders it unfavorable for UV/vis absorption via solar irradiation. Meanwhile, the presence of an intramolecular hydrogen bond has been confirmed in the *ortho*-dyes (**1**, **2**, and **3**) in both the solid state and solution, as testified by single-crystal X-ray diffraction, ^{1}H NMR, and DFT. This hydrogen bond is shown to be an important geometric causal factor in the ultimate nonfunctionality of *ortho*-dyes for DSSCs. The anchoring position of the −COOH group has been demonstrated to play the most crucial role in determining the DSSC performance of these dyes, while the different electron donors have, at best, a modest impact on DSSC efficiency. That said, these donors affect UV/vis absorption and dictate the nature of the crystal structures. Meanwhile, the performance of these dyes in DSSCs follows the order: *para*- > *meta*- > *ortho*-. The superiority of *para*-substituted azo dyes compared with both *meta*- and *ortho*-dyes are obvious. While the overall DSSC efficiencies of these specific azo dyes are modest on the absolute scale, it is the intrinsic capacity of the molecular design protocols of similar organic dyes for DSSC device performance and optical tenability, developed through this work, that is important. Such design protocols will facilitate the future molecular engineering of similar derivatives, specifically a −COOH group that resides at the *para*-position in these types of azo dyes is preferable

for DSSC device performance, while the nature of the electron donor substitution can be tailored to tune the UV/vis peak absorption wavelength and intensity of a given dye.

■ ASSOCIATED CONTENT

Supporting Information

List of bond lengths of *ortho*-dyes from XRD and DFT in gas and solution phase (Table S1). List of bond lengths of *para*-dyes from XRD and DFT in gas and solution phase (Table S2). Different resonance states of both *ortho*- and *para*-substituted benzene rings (Figure S1). Average values and errors for η, I_{sc}, V_{oc}, and FF with repeated fabrication and testing (Table S3). Average values for η, I_{sc}, V_{oc}, and FF according to different −COOH anchoring positions (Figure S2). IPCE curves for the seven azo dyes (Figure S3). UV/vis absorption spectra of the dyes as adsorbed onto TiO_2 nanoparticles (Figure S4). This material is available free of charge via the Internet at http://pubs.acs.org.

■ AUTHOR INFORMATION

Corresponding Author

*E-mail: jmc61@cam.ac.uk. Tel: +44 (0)1223 337470. Fax: +44 (0)1223 337356.

Notes

The authors declare no competing financial interest.

■ ACKNOWLEDGMENTS

J.M.C. thanks the Royal Society for a University Research Fellowship, the University of New Brunswick (UNB) for The UNB Vice-Chancellor's Research Chair, and NSERC for the Discovery Grant 355708 (for P.G.W.). K.S.L. acknowledges the EPSRC for a DTA Ph.D. studentship (EP/P505445/1). X.L. is indebted to the Singapore Economic Development Board for a Clean Energy Scholarship. The authors acknowledge support from the EPSRC UK National Service for Computational Chemistry Software (NSCCS), based at Imperial College London, and contributions from its staff in carrying out this work. The authors also thank Chi Hu for her technical assistance in NMR experiments.

■ REFERENCES

(1) O'Regan, B.; Grätzel, M. A low-cost, high-efficiency solar cell based on dye-sensitized colloidal TiO_2 films. *Nature* **1991**, *353*, 737−740.

(2) Anscombe, N. Solar cells that mimic plants. *Nat. Photonics* **2011**, *5*, 266−267.

(3) Robertson, N. Optimizing dyes for dye-sensitized solar cells. *Angew. Chem., Int. Ed.* **2006**, *45*, 2338−2345.

(4) Nazeeruddin, M. K.; De Angelis, F.; Fantacci, S.; Selloni, A.; Viscardi, G.; Liska, P.; Ito, S.; Takeru, B.; Grätzel, M. Combined experimental and DFT-TDDFT computational study of photoelectrochemical cell ruthenium sensitizers. *J. Am. Chem. Soc.* **2005**, *127*, 16835−16847.

(5) Persson, P.; Lundqvist, M. J. Calculated structural and electronic interactions of the ruthenium dye N3 with a titanium dioxide nanocrystal. *J. Phys. Chem. B* **2005**, *109*, 11918−11924.

(6) Anthonysamy, A.; Lee, Y.; Karunagaran, B.; Ganapathy, V.; Rhee, S.-W.; Karthikeyan, S.; Kim, K. S.; Ko, M. J.; Park, N.-G.; Ju, M.-J.; Kim, J. K. Molecular design and synthesis of ruthenium(II) sensitizers for highly efficient dye-sensitized solar cells. *J. Mater. Chem.* **2011**, *21*, 12389−12397.

(7) Millington, K. R.; Fincher, K. W.; King, A. L. Mordant dyes as sensitisers in dye-sensitised solar cells. *Sol. Energ. Mat. Sol. C.* **2007**, *91*, 1618−1630.

(8) Hara, K.; Sato, T.; Katoh, R.; Furube, A.; Ohga, Y.; Shinpo, A.; Suga, S.; Sayama, K.; Sugihara, H.; Arakawa, H. Molecular design of coumarin dyes for efficient dye-sensitized solar cells. *J. Phys. Chem. B* **2003**, *107*, 597−506.

(9) Kim, S.; Lee, J. K.; Kang, S. O.; Ko, J.; Yum, J.-H.; Fantacci, S.; De Angelis, F.; Di Censo, D.; Nazeeruddin, M. K.; Grätzel, M. Molecular engineering of organic sensitizers for solar cell applications. *J. Am. Chem. Soc.* **2006**, *128*, 16701−16707.

(10) Wu, Y.; Marszalek, M.; Zakeeruddin, S. M.; Zhang, Q.; Tian, H.; Grätzel, M.; Zhu, W. High-conversion-efficiency organic dye-sensitized solar cells: molecular engineering on D-A-π-A featured organic indoline dyes. *Energy Environ. Sci.* **2012**, *5*, 8261.

(11) Ooyama, Y.; Inoue, S.; Asada, R.; Ito, G.; Kushimoto, K.; Komaguchi, K.; Imae, I.; Harima, Y. Dye-sensitized solar cells based on a novel fluorescent dye with a pyridine ring and a pyridinium dye with the pyridinium ring forming strong interactions with nanocrystalline TiO_2 films. *Eur. J. Org. Chem.* **2010**, *2010*, 92−100.

(12) De Angelis, F.; Fantacci, S.; Selloni, A.; Nazeeruddin, M. K.; Grätzel, M. Time-dependent density functional theory investigations on the excited states of Ru(II)-dye-sensitized TiO_2 nanoparticles: The role of sensitizer protonation. *J. Am. Chem. Soc.* **2007**, *129*, 14156−14157.

(13) Liu, X.; Cole, J. M.; Waddell, P. G.; Lin, T.-C. Molecular origins of commercial laser dye functionality in azacoumarins and 2-quinolones: LD 425, LD 489 and LD 473. *Acta Crystallogr., Sect. B: Struct. Sci.* **2011**, *67*, 1−9.

(14) Le Bahers, T.; Pauporté, T.; Scalmani, G.; Adamo, C.; Ciofini, I. A TD-DFT investigation of ground and excited state properties in indoline dyes used for dye-sensitized solar cells. *Phys. Chem. Chem. Phys.* **2009**, *11*, 11276−11284.

(15) Clifford, J. N.; Martínez-Ferrero, E.; Viterisi, A.; Palomares, E. Sensitizer molecular structure-device efficiency relationship in dye sensitized solar cells. *Chem. Soc. Rev.* **2011**, *40*, 1635−1646.

(16) Wu, Y.; Zhang, X.; Li, W.; Wang, Z.-S.; Tian, H.; Zhu, W. Hexylthiophene-featured D-A-π-A structural indoline chromophores for coadsorbent-free and panchromatic dye-sensitized solar cells. *Adv. Energy Mater.* **2012**, *2*, 149−156.

(17) Hagfeldt, A.; Boschloo, G.; Sun, L.; Kloo, L.; Pettersson, H. Dye-sensitized solar cells. *Chem. Rev.* **2010**, *110*, 6595−6663.

(18) Fischer, M. K. R.; Wenger, S.; Wang, M.; Mishra, A.; Zakeeruddin, S. M.; Grätzel, M.; Bäuerle, P. D-π-A sensitizers for dye-sensitized solar cells: Linear vs branched oligothiophenes. *Chem. Mater.* **2010**, *22*, 1836−1845.

(19) Hagberg, D. P.; Marinado, T.; Karlsson, K. M.; Nonomura, K.; Qin, P.; Boschloo, G.; Brinck, T.; Hagfeldt, A.; Sun, L. Tuning the HOMO and LUMO energy levels of organic chromophores for dye sensitized solar cells. *J. Org. Chem.* **2007**, *72*, 9550−9556.

(20) Liu, X.; Cole, J. M.; Low, K. S. Molecular origins of dye aggregation and complex formation effects in coumarin 343. *J. Phys. Chem. C* **2013**, *117*, 14723−14730.

(21) Pfattner, R.; Pavlica, E.; Jaggi, M.; Liu, S.-X.; Decurtins, S.; Bratina, G.; Veciana, J.; Mas-Torrent, M.; Rovira, C. Photo-induced intramolecular charge transfer in an ambipolar field-effect transistor based on a π-conjugated donor−acceptor dyad. *J. Mater. Chem. C* **2013**, *1*, 3985.

(22) Mohammadi, A.; Yazdanbakhsh, M. R.; Farahnak, L. Synthesis and evaluation of changes induced by solvent and substituent in electronic absorption spectra of some azo disperse dyes. *Spectrochim. Acta, Part A* **2012**, *89*, 238−242.

(23) Almeida, M. R.; Stephani, R.; Dos Santos, H. F.; De Oliveira, L. F. C. Spectroscopic and theoretical study of the "azo"-dye E124 in condensate phase: Evidence of a dominant hydrazo form. *J. Phys. Chem. A* **2010**, *114*, 526−534.

(24) Charlton, M. H.; Docherty, R.; McGeein, D. J.; Morley, J. O. Theoretical investigation of the structure and spectra of donor-acceptor azobenzenes. *J. Chem. Soc., Faraday Trans.* **1993**, *89*, 1671−1675.

(25) Zhao, C. A theoretical study on the hyperpolarizabilities of dicyanovinyl and tricyanovinyl substituted benzenes, stilbenes,

styrenes and azobenzenes. *J. Mol. Struct.: THEOCHEM* **1996**, *367*, 73−82.
(26) Olmsted, J.; Lawrence, J.; Yee, G. G. Photochemical storage potential of azobenzenes. *Solar Energy* **1983**, *30*, 271−274.
(27) Mikroyannidis, J. A.; Tsagkournos, D. V.; Balraju, P.; Sharma, G. D. Low band gap dyes based on 2-styryl-5-phenylazo-pyrrole: synthesis and application for efficient dye-sensitized solar cells. *J. Power Sources* **2011**, *196*, 4152−4161.
(28) Nakajima, K.; Ohta, K.; Katayanagi, H.; Mitsuke, K. Photo-excitation and electron injection processes in azo dyes adsorbed on nanocrystalline TiO_2 films. *Chem. Phys. Lett.* **2011**, *510*, 228−233.
(29) Dalton, L. R.; Sullivan, P. A.; Bale, D. H. Electric field poled organic electro-optic materials: state of the art and future prospects. *Chem. Rev.* **2010**, *110*, 25−55.
(30) Loucif-Saibi, R.; Nakatani, K.; Delaire, J. A.; Dumont, M.; Sekkat, Z. Photoisomerization and second harmonic generation in disperse red one-doped and -functionalized poly(methy1 methacrylate) films. *Chem. Mater.* **1993**, *5*, 229−236.
(31) Rochford, J.; Chu, D.; Hagfeldt, A.; Galoppini, E. Tetrachelate porphyrin chromophores for metal oxide semiconductor sensitization: Effect of the spacer length and anchoring group position. *J. Am. Chem. Soc.* **2007**, *129*, 4655−4665.
(32) Jiang, X.; Karlsson, K. M.; Gabrielsson, E.; Johansson, E. M. J.; Quintana, M.; Karlsson, M.; Sun, L.; Boschloo, G.; Hagfeldt, A. Highly efficient solid-state dye-sensitized solar cells based on triphenylamine dyes. *Adv. Funct. Mater.* **2011**, *21*, 2944−2952.
(33) Rochford, J.; Galoppini, E. Zinc(II) tetraarylporphyrins anchored to TiO_2, ZnO, and ZrO_2 nanoparticle films through rigid-rod linkers. *Langmuir* **2008**, *24*, 5366−5374.
(34) Ma, T.; Inoue, K.; Yao, K.; Noma, H.; Shuji, T.; Abe, E.; Yu, J.; Wang, X.; Zhang, B. Photoelectrochemical properties of TiO_2 electrodes sensitized by porphyrin derivatives with different numbers of carboxyl groups. *J. Electroanal. Chem.* **2002**, *537*, 31−38.
(35) Ooyama, Y.; Inoue, S.; Nagano, T.; Kushimoto, K.; Ohshita, J.; Imae, I.; Komaguchi, K.; Harima, Y. Dye-sensitized solar cells based on donor-acceptor π-conjugated fluorescent dyes with a pyridine ring as an electron-withdrawing anchoring group. *Angew. Chem., Int. Ed.* **2011**, *123*, 7567−7571.
(36) Brewster, T. P.; Konezny, S. J.; Sheehan, S. W.; Martini, L. A.; Schmuttenmaer, C. A.; Batista, V. S.; Crabtree, R. H. Hydroxamate anchors for improved photoconversion in dye-sensitized solar cells. *Inorg. Chem.* **2013**, *52*, 6752−6764.
(37) McNamara, W. R.; Milot, R. L.; Song, H.; Snoeberger, R. C., III; Batista, V. S.; Schmuttenmaer, C. A.; Brudvig, G. W.; Crabtree, R. H. Water-stable, hydroxamate anchors for functionalization of TiO_2 surfaces with ultrafast interfacial electron transfer. *Energy Environ. Sci.* **2010**, *3*, 917.
(38) Giribabu, L.; Kanaparthi, R. K. Are porphyrins an alternative to ruthenium (II) sensitizers for dye-sensitized solar cells? *Curr. Sci.* **2013**, *104*, 847−855.
(39) Hart, A. S.; Chandra, B. K. C.; Gobeze, H. B.; Sequeira, L. R.; D'Souza, F. Porphyrin-sensitized solar cells: effect of carboxyl anchor group orientation on the cell performance. *ACS Appl. Mater. Interfaces* **2013**, *5*, 5314−5323.
(40) Hathaway, B. A. In *Organic Chemistry*, 5th ed.; Graham Solomons, T. W., Ed.; John Wiley & Sons, Inc.: New York, 1992; Vol. *69*, p A251.
(41) Wu, D. G.; Ghabboun, J.; Martin, J. M. L.; Cahen, D. Tuning of Au/n-GaAs diodes with highly conjugated molecules. *J. Phys. Chem. B* **2001**, *105*, 12011−12018.
(42) *CrystalClear-SM Expert and Crystal Structure*; Rigaku : The Woodlands, TX, 2009.
(43) Higashi T. *ABSCOR*, 1995.
(44) Farrugia, L. J. WinGX suite for small-molecule single-crystal crystallography. *J. Appl. Crystallogr.* **1999**, *32*, 837−838.
(45) Sheldrick, G. M. *SHELX97*: Programs for Crystal Structure analysis, **1997**.
(46) (a) Moreiras, D.; Solans, J.; Miravitlles, C.; Germain, G.; Declercq, J. P. *Cryst. Struct. Commun.* (refcode MAAZCZ), CCDC: Cambridge, U.K., 2004. (b) Lovell, S. Private Communication (refcode 143646), CCDC: Cambridge, U.K., 2004.
(47) Frisch, M. J.; Trucks, G. W.; Schlegel, H. B.; Scuseria, G. E.; Robb, M. A.; Cheeseman, J. R.; Scalmani, G.; Barone, V.; Mennucci, B.; Petersson, G. A.; Nakatsuji, H.; Caricato, M.; Li, X.; Hratchian, H. P.; Izmaylov, A. F.; Bloino, J.; Zheng, G.; Sonnenb, D. J. Gaussian 09, Revision B 01; Gaussian, Inc.: Wallingford, CT, 2009.
(48) Becke, A. D. Density-functional thermochemistry. III. The role of exact exchange. *J. Chem. Phys.* **1993**, *7*, 5648−5652.
(49) Rassolov, V. A.; Ratner, M. A.; Pople, J. A.; Redfern, P. C.; Curtiss, L. A. 6-31G* basis set for third-row atoms. *J. Comput. Chem.* **2001**, *22*, 976−984.
(50) Perdew, J.; Burke, K.; Ernzerhof, M. Generalized gradient approximation made simple. *Phys. Rev. Lett.* **1996**, *77*, 3865−3868.
(51) Boese, A.; Martin, J. Development of density functionals for thermochemical kinetics. *J. Chem. Phys.* **2004**, *121*, 3405−3416.
(52) Zakrzewski, V. G.; Von Niessen, W. Vectorizable algorithm for green function and many-body perturbation methods. *J. Comput. Chem.* **1993**, *14*, 13−18.
(53) Miertuš, S.; Scrocco, E.; Tomasi, J. Electrostatic interaction of a solute with a continuum. A direct utilizaion of ab initio molecular potentials for the prevision of solvent effects. *Chem. Phys.* **1981**, *55*, 117−129.
(54) Foresman, J. B.; Keith, T. A.; Wiberg, K. B.; Snoonian, J.; Frisch, M. J.; Incorporated, L.; Avenue, W.; Haven, N. Solvent effects. 5. Influence of cavity shape, truncation of electrostatics, and electron correlation on ab initio reaction field calculations. *J. Phys. Chem.* **1996**, *3654*, 16098−16104.
(55) Bernstein, J.; Davis, R. E.; Shimoni, L.; Chang, N.-L. Patterns in hydrogen bonding: Functionality and graph set analysis in crystals. *Angew. Chem., Int. Ed. Engl.* **1995**, *34*, 1555−1573.
(56) Etter, M. C. Encoding and decoding hydrogen-bond patterns of organic compounds. *Acc. Chem. Res.* **1990**, *23*, 120−126.
(57) Griffiths, J.; Feng, K. The influence of intramolecular hydrogen bonding on the order parameter and photostability properties of dichroic azo dyes in a nematic liquid crystal host. *J. Mater. Chem.* **1999**, *9*, 2333−2338.
(58) Oziminski, W. P.; Krygowski, T. M. Natural bond orbital (NBO) analysis of the angular group induced bond alternation (AGIBA) substituent effect. *J. Phys. Org. Chem.* **2010**, *23*, 551−556.
(59) Cole, J. M.; Waddell, P. G.; Jayatilaka, D. Solid-state dilution of dihydroxybenzophenones with 4,13-diaza-18-crown-6 for photocrystallographic studies. *Cryst. Growth Des.* **2012**, *12*, 2277−2287.
(60) Allen, F. H.; Watson, D. G.; Brammer, L.; Orpen, A. G.; Taylor, R. Typical interatomic distances: Organic compounds. In *International Tables for Crystallography*; International Union of Crystallography: Chester, England, 2006; Vol. *A*, pp 790−811.
(61) Allen, F. H.; Kennard, O.; Watson, D. G.; Brammer, L.; Orpen, A. G.; Taylor, R. Tables of bond lengths determined by X-ray and neutron diffraction. Part 1. Bond lengths in organic compounds. *J. Chem. Soc., Perkin Trans. 1* **1987**, S1−S18.
(62) Srinivasa Gopalan, R.; Kulkarni, G. U.; Ravi, M.; Rao, C. N. R. A charge density study of an intramolecular charge-transfer quinoid compound with strong NLO properties. *New J. Chem.* **2001**, *25*, 1108−1110.
(63) Cole, J. M. Organic materials for second-harmonic generation: Advances in relating structure to function. *Philos. Trans. R. Soc., A* **2003**, *361*, 2751−2770.
(64) Liu, X.; Cole, J. M.; Waddell, P. G.; Lin, T.-C.; Radia, J.; Zeidler, A. Molecular origins of optoelectronic properties in coumarin dyes: toward designer solar cell and laser applications. *J. Phys. Chem. A* **2012**, *116*, 727−737.
(65) Hatice, A. E. *Biodegradation of Azo Dyes*; Springer-Verlag: Berlin, Heidelberg, 2010; p 9.
(66) Xu, W.; Peng, B.; Chen, J.; Liang, M.; Cai, F. New triphenylamine-based dyes for dye-sensitized solar cells. *J. Phys. Chem. C* **2008**, *112*, 874−880.
(67) Peter, L. M. Dye-sensitized nanocrystalline solar cells. *Phys. Chem. Chem. Phys.* **2007**, *9*, 2630−2642.

(68) Thavasi, V.; Renugopalakrishnan, V.; Jose, R.; Ramakrishna, S. Controlled electron injection and transport at materials interfaces in dye sensitized solar cells. *Mat. Sci. Eng. R* **2009**, *63*, 81−99.
(69) Preat, J.; Michaux, C.; Jacquemin, D.; Perpéte, E. A. Enhanced efficiency of organic dye-sensitized solar cells: Triphenylamine derivatives. *J. Phys. Chem. C* **2009**, *113*, 16821−16833.
(70) Kalyanasundaram, K. *Dye-Sensitized Solar Cells*; EPFL Press: Lausanne, Switzerland, 2010; p 19.
(71) Dreuw, A.; Head-Gordon, M. Failure of time-dependent density functional theory for long-range charge-transfer excited states: The zincbacteriochlorin-bacteriochlorin and bacteriochlorophyll-spheroidene complexes. *J. Am. Chem. Soc.* **2004**, *126*, 4007−4016.
(72) Besombes, S.; Utille, J.-P.; Mazeau, K.; Robert, D.; Taravel, F. R. Conformational study of a guaiacyl beta-O-4 lignin model compound by NMR. Examination of intramolecular hydrogen bonding interactions and conformational flexibility in solution. *Magn. Reson. Chem.* **2004**, *42*, 337−347.
(73) Bekiroglu, S.; Kenne, L.; Sandström, C. ^{1}H NMR studies of maltose, maltoheptaose, alpha-, beta-, and gamma-cyclodextrins, and complexes in aqueous solutions with hydroxy protons as structural probes. *J. Org. Chem.* **2003**, *68*, 1671−1678.
(74) Sigalov, M.; Shainyan, B.; Chipanina, N.; Ushakov, I.; Shulunova, A. Intra- and intermolecular N-H...O hydrogen bonds in pyrrolyl derivatives of Indane-1,3-dione-experimental and theoretical study. *J. Phys. Org. Chem.* **2009**, *22*, 1178−1187.
(75) Leeflang, B. R.; Vliegenthart, J. F. G.; Kroon-Batenburg, L. M. J.; Van Eijck, B. P.; Kroon, J. A 1H-NMR and MD Study of intramolecular hydrogen bonds in methyl β-cellobioside. *Carbohydr. Res.* **1992**, *230*, 41−61.
(76) Gutierrez, J. A.; Falcone, R. D.; Silber, J. J.; Correa, N. M. Role of the medium on the C343 inter/intramolecular hydrogen bond interactions. An absorption, emission, and HNMR investigation of C343 in benzene/n-heptane mixtures. *J. Phys. Chem. A* **2010**, *114*, 7326−7330.
(77) Kroon, J.; Kroon-Batenburg, L. M. J.; Leeflang, B. R.; Vliegenthart, J. F. G. Intramolecular versus intermolecular hydrogen bonding in solution. *J. Mol. Struct.* **1994**, *322*, 27−31.
(78) Vittadini, A.; Selloni, A.; Rotzinger, F. P.; Grätzel, M. Formic acid adsorption on dry and hydrated TiO_2 anatase (101) surfaces by DFT calculations. *J. Phys. Chem. B* **2000**, *104*, 1300−1306.
(79) Sánchez-de-Armas, R.; San-Miguel, M. A.; Oviedo, J.; Márquez, A.; Sanz, J. F. Electronic structure and optical spectra of catechol on TiO_2 nanoparticles from real time TD-DFT simulations. *Phys. Chem. Chem. Phys.* **2011**, *13*, 1506−1514.
(80) Gong, X.-Q.; Selloni, A.; Vittadini, A. Density functional theory study of formic acid adsorption on anatase TiO_2(001): Geometries, energetics, and effects of coverage, hydration, and reconstruction. *J. Phys. Chem. B* **2006**, *110*, 2804−2811.
(81) Dean, J. A. *Lange's Handbook of Chemistry*, 15th ed.; McGraw-Hill, Inc.: New York, 1999; pp 91−98.
(82) Mack, J.; Stillman, M. J. Assignment of the optical spectrum of metal porphyrin and phthalocyanine radical anions. *J. Porphyrins Phthalocyanines* **2001**, *05*, 67−76.
(83) Kantchev, E. A. B.; Norsten, T. B.; Sullivan, M. B. Time-dependent density functional theory (TDDFT) modelling of Pechmann dyes: From accurate absorption maximum prediction to virtual dye screening. *Org. Biomol. Chem.* **2012**, *10*, 6682−6692.
(84) Guthrie, J. P.; Povar, I. A test of various computational solvation models on a set of "difficult" organic compounds. *Can. J. Chem.* **2009**, *87*, 1154−1162.
(85) Pastore, M.; De Angelis, F. Computational modelling of TiO_2 surfaces sensitized by organic dyes with different anchoring groups: Adsorption modes, electronic structure and implication for electron injection/Recombination. *Phys. Chem. Chem. Phys.* **2012**, *14*, 920−928.
(86) Clifford, J. N.; Palomares, E.; Nazeeruddin, M. K.; Grätzel, M.; Nelson, J.; Li, X.; Long, N. J.; Durrant, J. R. Molecular control of recombination dynamics in dye-sensitized nanocrystalline TiO_2 films: Free energy vs distance dependence. *J. Am. Chem. Soc.* **2004**, *126*, 5225−5233.